v1: 4 June 2024

Research Article

Dose Reduction in Medical Radiography: Advancing Veterinary Diagnostic Solutions

Huseyin Yavuz Kocaova[1], Nina Tunçel[2,1], Nuri Unal[3]

1. Department of Physics, Akdeniz University, Turkey; 2. Akdeniz University Hospital, Antalya, Turkey; 3. Akdeniz University, Turkey

Preprinted: 25 May 2024
Peer-approved: 4 June 2024

Qeios, Vol. 6 (2024)
ISSN: 2632-3834

In this study, we investigated photon attenuation using an anti-scatter lead grid with a flat panel detector (FPD) and aimed to mitigate it by implementing a linear array detector (LAD). We developed a mechanical system that facilitates X-ray scans using the LAD. For comparison, we selected a standard FPD unit. To assess the differences in entrance skin dose (ESD) between the LAD and FPD systems, we initially utilized anthropomorphic phantoms, followed by water phantoms for exposure tests. Results showed that at a water depth of 10 cm, the ESD from the LAD was 22% lower than that from the FPD. At 30 cm, this ratio increased up to 40%. As water thickness increased, the benefits of using the LAD became more evident, demonstrated by a lower ESD. This finding highlights the potential utility of implementing this equipment in veterinary radiography, particularly for imaging animals and their anatomical sites with thicker tissues.

Correspondence: papers@team.qeios.com — Qeios will forward to the authors

1. Introduction

X-ray imaging is crucial for diagnosing medical conditions, but it comes with the risk of ionizing radiation exposure. While advancements in technology aim to reduce this risk, it is important for both healthcare providers and patients to be aware of and minimize unnecessary exposure to radiation during diagnostic procedures. During X-ray diagnostics, patients also receive ionizing radiation. Nowadays, a significant part of the total dose in our daily lives is due to the increase in X-ray imaging [1][2][3]. In developed countries, individuals typically receive an average radiation dose of 0.2 to 2.2 millisieverts (mSv) per year from X-rays [4]. In routine diagnostic imaging examinations such as mammography, the dose becomes even more important [5]. In veterinary radiography, scintigraphy, and ultrasonography are frequently utilized for diagnosing conditions in equine and cattle, particularly when conventional X-ray equipment faces challenges or limitations, such as regulatory constraints or difficulties in imaging beyond the extremities of these large animals [6][7][8].

In physics, attenuation refers to the reduction in the intensity of a signal or beam as it passes through a medium and is explained by the Beer-Lambert Law as $I_1=I_0 e^{-(\mu.x)}$, where I_0 is the incident, I_1 is the transmitted intensities, μ is the linear

 doi.org/10.32388/X7CKJS.3

attenuation coefficient, and *x* is the distance that the photon travels through the medium. In radiology, attenuation can be explained as intensity and dose, where the medium is the tissue. Intensity attenuation refers to the reduction in the intensity of the beam as it passes through the tissue, while dose attenuation refers to the reduction in the amount of radiation absorbed by tissue as it passes through it. In this study, we emphasized the intensity attenuation by the anti-scatter grid as a reference to ESD measurements.

The effects of radiation on living cells can be summarized through two primary mechanisms: direct and indirect adverse effects [9][10][11][12]. Direct effects occur when radiation ionizes DNA atoms, potentially causing considerable damage. If extensive, this damage can prevent proper chromosome replication or alter DNA information, leading to cell death due to direct ionization [13]. Since living cells are primarily composed of water, radiation interacts with it, leading to indirect effects by producing radicals such as H, OH, and, in the final toxic form, H_2O_2 [14][15][16]. Given these risks, current research is focused on designing novel devices that reduce radiation dose while maintaining sufficient image quality for diagnostic purposes.

Like all other imaging concepts, digital detectors have replaced conventional films in medical imaging. Initially, computed radiography (CR) [17] using the photostimulable storage method was introduced, followed by the widespread adoption of flat panel detectors (FPD) in X-ray diagnostics [18][19][20]. There are two primary types of FPD based on their construction specifications: direct and indirect. In a direct detector, there is an outer amorphous selenium (a-Se) layer with a dipole structure. The incident X-ray photon is directly converted into an electric charge by forming an electron-vacancy ion pair in the a-Se layer and creates a current. This current is proportional to the photon's energy; it is detected and converted into an image by a thin film transistor (TFT) array [21]. Indirect-type FPD detectors have a scintillator layer of Cesium Iodide (CsI) or Gadolinium Oxysulfide (Gd_2O_2S) on top. This converts X-rays into light photons. Beneath this layer, there are the Amorphous Silicon (a-Si) photodiodes on a TFT array [22][23]. A flat panel detector (FPD) has a two-dimensional photosensitive area. The collimated X-ray beam is directed towards the object in a cone-shaped geometry. The type of beam geometry being referred to is known as a cone beam. An anti-scatter grid is placed in front of the FPD.

The grid is a plate with Pb sections in a membrane structure used to improve image quality. When an incident X-ray arrives at the patient, part of it is scattered from bones or tissue, as shown in Fig.1A. An anti-scatter grid is designed to prevent those scattered photons from reaching the detector [24][25]. Since incident rays are in a cone shape, the grid is designed to allow direct photons. That is why grids have a source to image distance (SID) [26]. The use of a grid is mandatory, especially when tissue thickness is increased [27][28]. Using an anti-scatter grid can increase the patient's entrance dose because the primary beam may require an increase in intensity to compensate for the absorption of X-rays by the grid. The decision to use an anti-scatter grid thus involves a trade-off between reducing scatter (by enhancing image quality) and minimizing the radiation dose to the patient [29]. That requires careful consideration to balance these factors appropriately. Managing and minimizing this dose are crucial for patient safety, as excessive radiation can increase the risk of harm and potential long-term effects, such as cancer [30][31].

In the LAD system, the incident X-ray and the detector's active area are in the same plane, and the image is performed line by line to form the image, as shown in Fig.1B. The X-ray is fan-shaped and covers the photosensitive window of the LAD. In this case, the scattered photons can't reach the detector to distort the image, and an anti-scatter grid is not required [32].

Due to the possible vibrations caused by scan movement and time elapse, LAD is not yet widely used in direct radiography. Moreover, scan time should be well arranged considering patient-oriented motion artifacts.

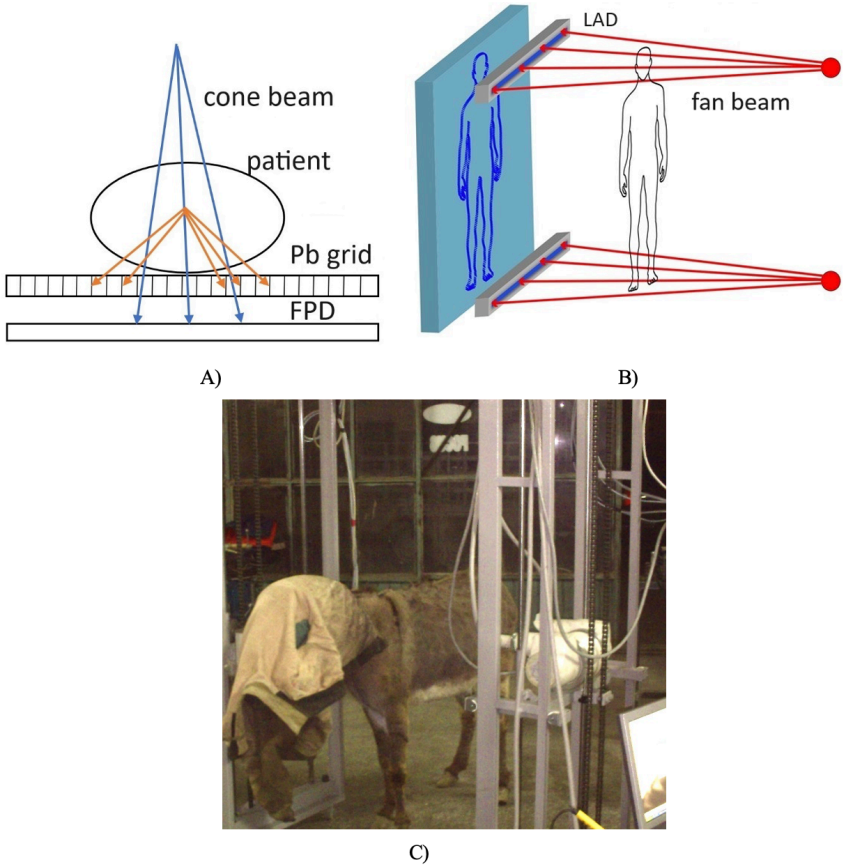

Figure 1. A) FPD and anti-scatter Pb grid, which attenuates scattered photons from the cone beam and lets direct photons form the image. B) LAD with fan beam. C) Four-year-old female donkey.

That is why LADs are widespread in non-destructive testing (NDT) and security areas where the LAD and X-ray source are fixed while the object moves on a conveyor [33].

Our prior aim was to perform a study that helps reduce ESD in radiography. When we observed the dose reduction that is especially related to the thickness of the tissue in LAD, we evaluated veterinary radiography where thicker tissues should be diagnosed. That is why we firstly described how medical studies were performed by using anthropomorphic human and water phantoms, then continued in veterinary diagnostics by imaging a four-year-old female donkey, as shown in Fig. 1C.

doi.org/10.32388/X7CKJS.3

2. Materials and Methods

To improve the reliability of the study, all the physical and X-ray features of the LAD system in Fig.1C were designed and manufactured according to the reference FPD system. Both LAD and FPD were chosen as indirect (a-Si) photodiode array types with a Gadolinium Oxysulfide scintillator.

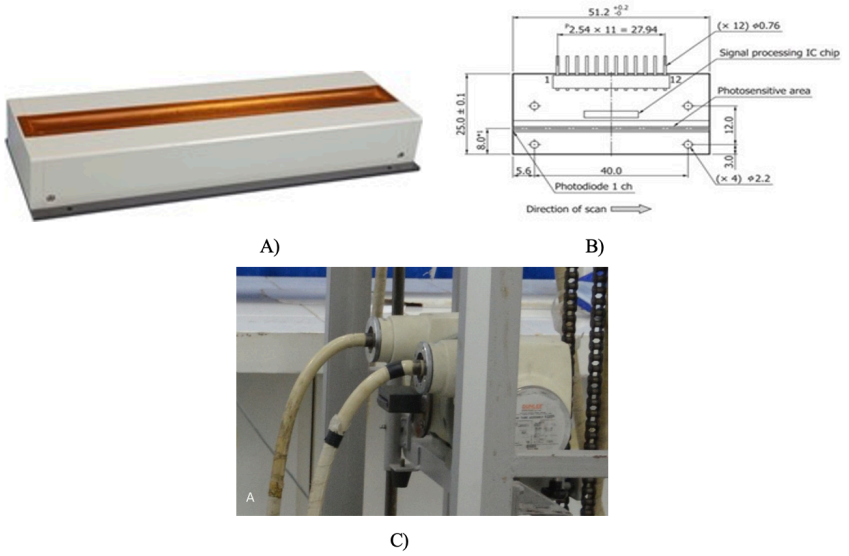

Figure 2. A) Hamamatsu C9750T line scan camera B) One piece of linear array detector in Hamamatsu C9750T C) Pb fan beam collimator attached to the X-ray tube.

The X-ray tube and LAD were mounted on the same horizontal plane on quadruple bearings so that an X-ray scan could be performed at any selected height from 20-210 cm and at speeds up to 1.2 m/s robotically. The source to image distance (SID) was chosen as 120 cm, similar to the FPD reference system.

As the LAD, the Hamamatsu C9750T line scan camera (Fig.2A) was used [34]. In fact, this detector was built for NDT applications; however, the specifications covered the range of direct radiography examinations from 25 to 160 kVp. In direct radiography, a single image is obtained, whereas in fluoroscopy, a series of images are captured to create a film for diagnostic purposes [35][36]. The key differences stem from the geometry of the introduced X-ray beam, as cone-shaped for FPD and fan-shaped for LAD. We emphasize that the C9750T captures line by line, resulting in a still radiographic but not fluoroscopic image, even though it was named as a line scan camera. One piece of the linear array detectors in the line scan camera is presented in Fig.2B. There are 10 pieces of detectors that make up 512 mm width of the total detection area in the camera. The whole image of the scanned area was created digitally. The maximum scan time was defined as 1200 ms experimentally. The purpose of faster scans is to avoid motion artifacts caused by patient movements. Imaging at a shorter time is especially important in pediatric imaging [37][38]. The fan beam collimator (Fig.2C) was designed and built from Pb by us so that a fan beam at equal width to the LAD's photosensitive area would be projected. Therefore, the X-ray source and LAD made simultaneous vertical movement according to the selected

doi.org/10.32388/X7CKJS.3

anatomical site. The LAD X-ray unit was composed of a Trex TM-80 radiographic fluoroscopic (RF) high voltage (HV) generator (150 kVp – 10.000 mAs), a Varian Rad 60 tube with 0.6 mm / 1.2 mm focal spots in a Sapphire housing, Varex N4X high voltage cables, and a Hamamatsu C9750 line scan camera with a 200 µm pixel size and 12-bit grayscale spatial resolution.

The reference was the DR RAD X3C Nova FA FPD system, which has a 50KW R generator, a Varian Rad 13 tube with 1.0 mm / 2.0 mm focal spots that is attached to a ceiling suspension with an auto collimator, a 17"X17" amorphous silicon detector with a 160 µm pixel size and 12-bit grayscale, a 96-157 cm SID, and a 10:1 ratio fixed anti-scatter grid.

The Best Medical brand TN-RD-90 MOSFET dosimeter was used to measure doses [39][40]. Dosimeter probes were placed on anthropomorphic phantoms and the water phantom for entrance skin dose (ESD) measurements [41]. These X-ray scans using the Nova FPD system were performed, and the dose measurements were done. In these exams, the RSD brand anthropomorphic RS 108 skull and RS 330 upper body phantoms were placed in front of the flat panel detector [42][43][44]. The image quality of X-ray parameters at each anatomical position was assessed by measuring the grayscale of a one cm^2 area at the center of the raw image, as recorded by Digital Imaging and Communications in Medicine (DICOM) software.

Based on these quality standards, the ideal X-ray exposure parameters for each site and position were established. For each position, such as skull Posterior-Anterior (PA) or lumbar Anterior-Posterior (AP), these reference exposure parameters were kept at the center of deviation, and ten more images were taken in the diagnostic grayscale range. We increased and decreased the kVp by 1-2 steps and recorded the AEC mAs. The average doses in mGy and exposure parameters such as kVp and mAs are shown in Table 1A.

According to the recorded grayscale, we made the same anthropomorphic phantom analysis by LAD similarly as shown in Fig.3A, 3B, and 3C. Since there was no AEC in LAD, X-ray parameters were chosen manually. Again, ten images were taken for each anatomical position and recorded as seen in Table 1B.

In dose and X-ray parameters, we should have made the right selections since in LAD the X-ray was in fan beam geometry instead of a cone. The MOSFET dosimeter had a point size sensor, and no calculation was necessary while the active scan area was chosen correctly in its settings. For the kVp and mAs selections, we used the central dose reference from FPD raw images and recorded kVp and mAs when we obtained the same grayscale by LAD. kVp values were written directly; however, mAs values were obtained by dividing the scan time. For example, if 70 kVp and 1000 mAs were selected by the Trex TM-80 RF LAD system's operator console and the scan was completed at 200 ms at our servo-controlled mechanical system console, the real mAs of each line of the total image was taken as 1000 / 200 = 5 mAs. It should be noted that in fan beam geometry, the X-rays were applied via a fan beam collimator as the width of a line, and each line was obtained by 5 mAs of the X-ray exposure.

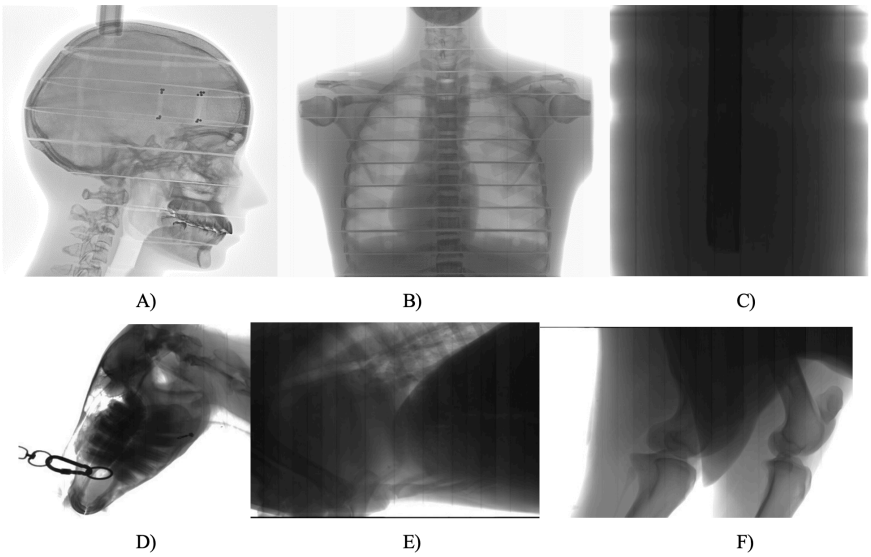

Figure 3. LAD images A) RS108 adult male anthropomorphic phantom skull lateral B) RS 330 adult male anthropomorphic phantom chest PA C) Water phantom at 60 cm water depth while the Aluminum bone model was barely recognizable D) Four years old female donkey skull E) Four years old female donkey lumbar F) Four years old female donkey knee.

In this case, our analogy was the image obtained at 70 kVp and 5 mAs. Afterwards, the water phantom was analyzed.

As the water phantom, a radiotransparent LEXAN sheet cabinet with a 20 mm layer of Aluminum (Al) block placed inside as a bone model was used to analyze water thickness from 10 to 60 cm. In each depth dependency examination, the depth was incrementally increased by 10 cm. Then we found the lowest X-ray parameters at which the Al bone model in water was barely visible by DICOM and recorded the doses with respect to the water depth. Afterwards, the procedure was repeated by the LAD system. These values are shown in Table 1C.

Finally, veterinary imaging using LAD was conducted. Observations indicated that the animal was startled by mechanical movements and sounds. To mitigate this, its eyes and ears were covered with a cloth, and mechanical noises were minimized through lubrication. This approach allowed for the acquisition of diagnostic images (Fig.3D, 3E, and 3F) under the X-ray parameters listed in Table.1D.

3. Results and Discussion

The ESD measured by MOSFET was averaged, and then the standard deviation was calculated for 10 repeated images captured by both the LAD and FPD, concerning the X-ray exposure of anthropomorphic phantoms. The units for the entrance skin dose and standard deviation are defined in milli-gray (mGy). The dose result values were presented in Table.1A and 1B, while the graphical comparison was plotted in Fig.4A based on these values. It was observed that there is a dramatic dose difference between the LAD and FPD in the lumbar AP and lumbar lateral (LAT) examinations. This highlights the requirement for higher kVp and mAs settings for imaging thicker tissues, as compared to the

settings used for skull and chest examinations with FPD. For the Skull PA, the ESD was 25.9% lower with the LAD, and for the lumbar LAT, there was a pronounced reduction of 43.6% compared to the FPD. The Pb membrane structure of the grid was causing a higher amount of photon attenuation when the thickness and dose rate according to the phantom's anatomical site and position were increased.

Anatomical site Anthropomorphic	MOSFET Dosimeter ESD (mGy)	Anatomical Program (kVp)	AEC (mAs)
Skull PA	1.36 ± 0.06	69 - 78	15 - 18
Skull Lateral	1.05 ± 0.07	63 - 65	10 -15
Chest PA	0.31 ± 0.09	78 - 85	7 - 9
Chest Lateral	0.65 ± 0.12	80 - 89	13 - 16
Lumbar AP	3.93 ± 0.04	75 - 83	27 - 34
Lumbar Lateral	6.71 ± 0.02	78 - 92	37 - 48

Table 1A. FPD doses and X-ray parameters

Anatomical site Anthropomorphic	MOSFET Dosimeter ESD (mGy)	Applied kVp	Applied mAs
Skull PA	1.08 ± 0.07	62 - 71	13 - 15
Skull Lateral	0.95 ± 0.08	58 - 63	9 - 12
Chest PA	0.29 ± 0.13	71 - 79	6 - 8
Chest Lateral	0.57 ± 0.11	74 - 81	8 - 11
Lumbar AP	2.87 ± 0.03	64 - 74	20 - 25
Lumbar Lateral	4.67 ± 0.02	68 -77	30 - 38

Table 1B. LAD doses and X-ray parameters

	10 cm	20 cm	30 cm	40 cm	50 cm	60 cm
LAD ESD (mGy)	0.95	2.98	5.32	14.74	37.48	72.76
FPD ESD (mGy)	1.18	3.85	7.45	31.45	122.34	-

Table 1C. LAD and FPD water phantom doses according to the water thickness

doi.org/10.32388/X7CKJS.3

Anatomical site veterinary	Applied kVp	Applied mAs
Skull	64 - 69	13 - 16
Chest	62 - 68	10 - 13
Vertebrae	67 - 76	25 - 33
Lumbar	69 - 78	32 - 44
Femur Oblique	77 - 85	40 - 47

Table 1D. Four years old donkey LAD X-ray parameters

An anthropomorphic phantom is designed to simulate the diagnostic features of an X-ray procedure. Obviously, anthropomorphic phantom dose analysis couldn't have given precise results since the gray scale and diagnostic quality phenomena are subjective criteria themselves [45]. However, as an idea about our goal, the dose comparison for the anatomical sites was obtained. On the other hand, a water phantom is used to determine X-ray doses precisely since water reacts to X-ray photons like tissue by means of absorption and scattering characteristics while it has a homogeneous structure [46][47]. To further refine our comparison of entrance doses between the use of the LAD and FPD, water phantom analysis was performed. Water phantom analysis can be considered alongside anthropomorphic phantom analysis, as it involves measuring the dose from photons that penetrate through homogeneous water and reach the detector in X-ray settings, including the presence of an aluminum block [48].

Image-related factors like grayscale or diagnostic quality were not taken into account in these water phantom measurements. At 10 cm of water thickness, the dose necessary for LAD was 22% lower than FPD, which could be considered in the range of mammography examinations. At a depth of 30 cm, the dose increased by 40%, and at 40 cm, this ratio surged to 113.3%. At 60 cm, neither the aluminum bone model was visible nor was the AEC able to terminate the exposure, resulting in the inability to obtain a dose value with the FPD. Photon attenuation on the grid increased correspondingly with higher doses. Even with the highest X-ray generator settings, an image could not be obtained, and AEC could not terminate the exposure. On the contrary, LAD performed successfully (as shown in Fig.3D). According to the entrance skin dose values from the X-ray settings for our water phantom examination, as mentioned in Table.1C, a graphical comparison for a more detailed analysis between the LAD and FPD is demonstrated in Fig.4B.

The dramatic ESD difference starting from 20 cm in Fig.4B can be explained as follows: As water thickness increased by 10 cm steps, the number of scattered, then attenuated photons by the grid increased respectively [49][50]. That is why, at 50 cm of water depth, FPD ESD was 326.4% higher than LAD. At 60 cm, FPD cannot get an image while LAD was obtained as shown in Fig.3C.

It was remarkable that the animal's anatomical sites and X-ray parameters for the LAD listed in Table.1D were quite similar to the FPD anthropomorphic phantom parameters in Table.1A. The results obtained using these X-ray

parameters indicated that adequate image quality could be achieved with correspondingly lower ESD. The close sizes of donkeys and horses suggest that, in theory, equine whole-body imaging could be successfully performed [51][52]. Considering this advantage and using an X-ray generator capable of delivering high voltages up to 150 kVp and 10,000 mAs, it is also theoretically possible to diagnose cattle.

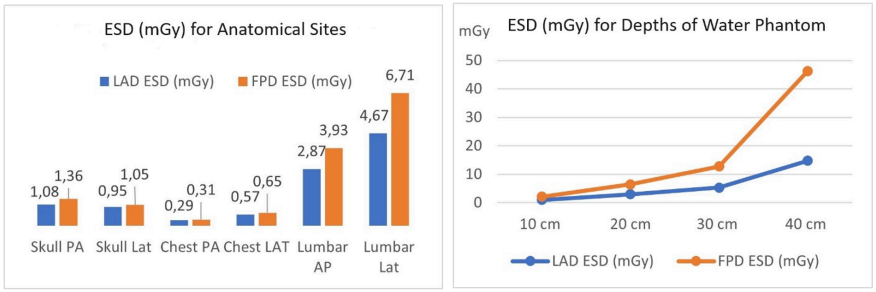

A) B)

Figure 4. A) Comparison of anthropomorphic phantom entrance skin doses by LAD and FPD. Measured LAD doses are 25.9 % in skull PA and 43.6 % in lumbar lateral lower than FPD. B) Comparison of water phantom doses by LAD and FPD. Measured LAD doses are 22 % at 10 cm, 40% at 30 cm lower than FPD.

The LAD system that we designed performs servo-controlled chain-driven movement on linear bearings. Although linear double bearings were designed to minimize mechanical vibration, still slight vibration had been observed. During LAD scans, vibration was not surprising considering the weight of the vertically moving system. This might be resembled to motion artifacts originated by a patient in computed tomography (CT) and despite these vibrations, diagnostic images could be taken [53][54]. In a mechanical design where vibrations are minimized, diagnostic image quality would be increased and ESD might be reduced respectively.

In addition to the dose reduction, magnification with the LAD detector brings a new opportunity. Again, in FPD mammography, magnification is performed even though a grid is used [55]. In FPD, the patient or object should lean on the grid; otherwise, diagnostic quality can't be obtained. However, in our studies with LAD, it has been observed that a higher magnification rate can be achieved by simply moving the object closer to the X-ray source without changing the X-ray parameters. In other words, the patient can be located far from the detector and closer to the X-ray source. In this circumstance, it is possible to perform higher magnification without loss in image quality. The magnification capability of LAD is a phenomenon that may require further research in direct radiography and mammography.

4. Conclusion

The potential for dose reduction offers benefits not only in human medicine but also in veterinary applications. Currently, X-ray imaging of cattle and equine species is typically difficult except for their extremities. However, our water phantom tests have demonstrated that full-body imaging of large animals is feasible using the LAD system with existing medical X-ray high voltage (HV)

generators and tubes. In our study, imaging of a donkey was achieved experimentally using the LAD system, and theoretically, it could be extended to equine and cattle imaging.

Currently, LAD technology is primarily utilized in non-destructive testing (NDT) and security applications, with only a few systems employed in medical radiography. Unlike NDT, where the object is typically stationary while the source and detector move, diagnostic imaging requires the patient to remain still during the imaging process. Our mechanical LAD system was specifically designed and built for experimental dose comparison purposes. During our tests with anthropomorphic phantoms, we achieved diagnostic-quality images, although slight mechanical vibrations were observed.

To further refine this technology for direct radiography applications such as mammography or trauma examinations, it is crucial to design and improve the mechanical structures used in LAD systems. By doing so, we could perform diagnostic imaging with significantly lower doses than those currently achieved with FPD systems. Low dose means low energy consumption, which may create the chance of producing mobile diagnostic equipment instead of stationary ones. Additionally, our experience during veterinary scanning highlighted the importance of minimizing noise and reducing scan time. For future systems, replacing chains with belts in the moving components could reduce noise, ensuring that animals remain calm and stationary during imaging. Moreover, a ceiling-suspended mechanical system could be more convenient. These adaptations may enhance the practicality and effectiveness of LAD systems in veterinary applications.

Statements and Declarations

Competing Interest

The authors declare that no competing interests exist.

Funding

The authors gratefully acknowledge the partial financial support from the Ministry of Industry and Technology B.14.2.KSG.4.07.00.00-150-1392 and the Akdeniz University Rectorate Scientific Research Center (AU-BAP-FYL1787).

Ethics

The animal study protocol was approved by the Local Ethical Committee, Antalya, Turkey. Procedures were conducted in accordance with the European Union Directive 63/2010/EU on the protection of animals used for scientific purposes.

Data Availability

The raw data supporting the conclusions of this article (e.g., dose measurements, exposure parameters) are available from the authors upon reasonable request. Inquiries can be directed to the corresponding author.

Author Contributions

Conceptualization: HYK, NT; Methodology: HYK; Software: HYK; Validation: HYK, NT, NU; Formal Analysis: NT; Investigation: HYK; Resources: NU; Data Curation:

HYK; Writing – Original Draft Preparation: HYK; Writing – Review & Editing: NT; Visualization: HYK; Supervision: NT; Project Administration: HYK; Funding Acquisition: NU.

References

1. ^*Marcu L, Minh Chau M, Bezak E (2021). "How much is too much? Systematic rev iew of cumulative doses from radiological imaging and the risk of cancer in child ren and young adults." Critical Reviews in Oncology /Hematology.* ***160****.*
2. ^*Winder M, Owczarek A, Chudek J, Kowalczyk J, Baron J (2021). "Are We Overdoin g It? Changes in Diagnostic Imaging Workload during the Years 2010–2020 inclu ding the Impact of the SARS-CoV-2 Pandemic." Healthcare (Basel, Switzerland).*
3. ^*Charles M (2000). "Sources and Effects of Ionizing Radiation." United Nations S cientific Committee on the Effects of Atomic Radiation UNSCEAR 609.*
4. ^*Keith S, Murray E, Spoo W (1999). "Sources of Population Exposure to Ionizing R adiation." Agency for Toxic Substances and Disease Registry ATSDR 243.*
5. ^*Bosmans H, Marshall N (2013). "Radiation doses and Risks Associated with Ma mmographic screening." Current Radiology Reports.* ***1****:30–38.*
6. ^*Butler J, Colles C, Dyson S, Kold S, Poulos P, Puchalski S (2017). "Grids." Clinical R adiology of the Horse. Chapter 1, 8.*
7. ^*Punsmann S, Hellige M, Hoppe J, Freise F, Venner M (2021). "Acute interstitial pn eumonia in foals: A severe, multifactorial syndrome with lung tissue recovery in s urviving foals." Equine Veterinary Journal.*
8. ^*Votion D, Vandenput S, Duvivier H, Art T, Lekeux P (1997). "Analysis of equine sci ntigraphical lung images." The Veterinary Journal.*
9. ^*Vaiserman A, Koliada A, Socol Y (2018). "Health Impacts of Low-Dose Ionizing R adiation: Current Scientific Debates and Regulatory Issues." Dose Response.*
10. ^*Nikitaki Z, Mavragani I, Laskaratou D, Gika V, Moskvin V, Theofilatos K (2016). S eminars in Cancer Biology.* ***37–38****:77-95.*
11. ^*Weiss G, Mossman K (2009). "Ionizing Radiation and Cancer." Radiation Resear ch.* ***2****(4).*
12. ^*Alizadeh E, Thomas M, Orlando, Sanche L (2015). "Biomolecular Damage Induc ed by Ionizing Radiation: The Direct and Indirect Effects of Low-Energy Electrons on DNA." Annual Review of Physical Chemistry.* ***66****.*
13. ^*Himmetoglu S, Guven F, Bilsel N, Dincer Y (2015). "DNA damage in children with scoliosis following X-ray exposure." Minerva Pediatrica.* ***67****:1-2.*
14. ^*Adhikari R (2012). "Effect And Application of Ionization Radiation (X-Ray) In Liv ing organism." The Himalayan Physics.* ***1-2****:89-92.*
15. ^*Reisz J, Bansal N, Qian J, Zhao W, Furdui C (2014). "Effects of Ionizing Radiation on Biological Molecules-Mechanisms of Damage and Emerging Methods of Dete ction." Antioxidants & Redox Signaling.* ***21****:260–292.*
16. ^*Wang W, Zengliang Y, Wenhui S (2010). "Ion irradiation and biomolecular radiat ion damage II. Indirect effect." Biological Physics.*
17. ^*Seeram S (2019). "Computed Radiography: Physics and Technology." Digital Rad iography. 41–63.*
18. ^*Cowen A, Kengyelics M, Davies A (2008). "Solid-state, flat-panel, digital radiogr aphy detectors and their physical imaging characteristics." Clinical Radiology.* ***63*** *(5):487-498.*
19. ^*Yaffe M, Rowlands J (1997). "X-ray detectors for digital radiography." Physics in Medicine & Biology.* ***42****:1–39.*

20. ^ *Seibert A (2006). "Flat-panel detectors: how much better are they?" Pediatric Radiology. **36**:173–181.*
21. ^ *Chen F, Wang K, Fang Y, Allec N, Belev G, Kasap S, Karim K (2011). "Direct-Conversion X-Ray Detector Using Lateral Amorphous Selenium Structure." IEEE Sensors Journal. **11**(2).*
22. ^ *Floyd C, Warp R, Dobbins J, Chotas H, Baydush H, Voracek R, Ravin C (2001). "Imaging Characteristics of an Amorphous Silicon Flat-Panel Detector for Digital Chest Radiography." Radiology. **218**(3).*
23. ^ *Paul G, Aufrichtig R (2000). "Performance of a 41×41amorphous silicon flat panel x-ray detector for radiographic imaging applications." Medical Physics.*
24. ^ *Lendl M (2007). "Optimized anti-scatter grids for flat panel detectors." Physics of Medical Imaging. **6510**.*
25. ^ *Chan H, Lam K, Wu Y (1990). "Studies of performance of ant scatter grids in digital radiography: Effect on signal-to-noise ratio." Medical Physics. **17**(4):655-664.*
26. ^ *Sabic I (2016). "The Effect of Anti-Scatter Grid on Radiation Dose in Chest Radiography in Children." Paediatrics Today. 75-80.*
27. ^ *Martin J (2007). "Optimization in general radiography." Biomed Imaging Intervention Journal.*
28. ^ *Kawashima H, Ichikawa K, Kitao A, Matsubara T, Sugiura T, Kobayashi T, Kobayashi S (2023). "Radiation dose considerations in digital radiography with an anti-scatter grid: A study using adult and pediatric phantoms." Medical Physics. **24**(9).*
29. ^ *Sigmund P (2014). "Part 3. Interatomic Potentials, Scattering and Nuclear Stopping." Particle Penetration and Radiation Effects. **2**:235-276.*
30. ^ *Linet M, Slovis T, Miller D, Kleinerman R, Lee C, Rajaman P, Gonzalez A (2012). "Cancer risks associated with external radiation from diagnostic imaging procedures." CA: A cancer journal of clinicians. **62**(2):75–100.*
31. ^ *Lin E (2010). "Radiation risk from medical imaging." Mayo Clinic Proceedings. **85**(12):1142-1146.*
32. ^ *Sones R, Lauro K, Cattell C (1990). "A detector for scanned projection radiography." Radiology. **175**(2).*
33. ^ *Wang J, Miao C, Wang W, Lu X (2007). "Research of x-ray nondestructive detector for high-speed running conveyor belt with steel wire ropes." Engineering, Physics.*
34. ^ *Hamamatsu (2016). "X-Ray Line Scan Camera C9750 at." HPK. No. SFAS0017E13.*
35. ^ *Krohmer S (1989). "Radiography and fluoroscopy, 1920 to the present." RadioGraphics. **9**(6).*
36. ^ *Seibert A (2019). "Projection X-ray imaging, radiography, mammography, fluoroscopy." Health Physics. **116**(2):148–156.*
37. ^ *Don S (2011). "Pediatric digital radiography summary overview: state of confusion." Pediatric Radiology. **41**:567–572.*
38. ^ *Hintenlang J, Williams L, Hintenlang E (2002). "A survey of radiation dose associated with pediatric plain-film chest X-ray examinations." Pediatric Radiology. **32**:771–777.*
39. ^ *Dance D (2014). "Chapter 21 Instrumentation for Dosimetry 21.4 Semiconductor Dosimeters." Diagnostic Radiology Physics A Handbook for Teachers and Students IAEA. 535-537.*
40. ^ *Huda W, Donnely K (2014). "Chapter 11 Radiation Dosimetry." RT X-Ray Physics Review. 251-275.*

41. ^Tanabe R, Araki F (2021). "Determination of the surface dose of a water phanto m using a semiconductor detector for diagnostic kilovoltage x-ray beams." Physic a Medica.
42. ^Bliznakova K, Buliev I, Bliznakov Z (2018). "Introduction to anthropomorphic ph antoms." 2-1, 2-40, 3-18.
43. ^Dewerd LA, Kissick M (2014). "The Phantoms of Medical and Health Physics De vices for Research and Development." 1-15, 89, 91-122.
44. ^Charnley C, England A (2016). "An option for optimizing the radiographic techni que for horizontal beam lateral (HBL) hip radiography when using digital X-ray equipment." Radiography. **22**(2):137-142.
45. ^Ma K, Hogg P, Tootell A, Manning D, Thomas N, Kane T, Kelly J, McKenzie M, Kit ching J (2013). "Anthropomorphic chest phantom imaging, The potential for dose creep in computed radiography." Radiography. **19**(3):207-211.
46. ^Gargett A, Briggs A, Booth J (2020). "Water equivalence of a solid phantom mate rial for radiation dosimetry applications." Physics Imaging Radiation Oncology. **1 4**:43-47.
47. ^Shikhaliev P (2012). "Dedicated phantom materials for spectral radiography an d CT." Physics in Medicine & Biology. **57**(6):1575.
48. ^Yadav N, Singh M, Mishra S (2021). "Tissue-equivalent materials used to develo p phantoms in radiation dosimetry." Materials Today: Proceedings. **47**(19):7170-71 73.
49. ^Ubeda C, Vano E, Gonzalez L, Miranda P (2012). "Influence of the antiscatter gri d on dose and image quality in pediatric interventional cardiology X-ray system s." CCI.
50. ^Söderman M, Hannson B, Axelsson B (1998). "Radiation Dose and Image Quality in Neuroangiography: Effects of Increased Tube Voltage, Added X-Ray Filtration a nd Antiscatter Grid Removal." Interventional Neuroradiology.
51. ^Mclean A (2014). "Comparing the physiological and biochemical parameters of mules and hinnies to horses and donkeys." academia.edu.
52. ^Dierendonck M, Burden F, Rickards K, Loon J (2020). "Monitoring Acute Pain in Donkeys with the Equine Utrecht University Scale for Donkeys Composite Pain As sessment (EQUUS-DONKEY-COMPASS) and the Equine Utrecht University Scale f or Donkey Facial Assessment of Pain (EQUUS-DONKEY-FAP)." Animals (Basel).
53. ^Murphy A, Hacking C, Iflaq P (2016). "Motion Artifact." Radiopaedia.org.
54. ^Sun X, Huang F, Lai G, Yu D, Zhang B, Guo B, Ma Z (2021). "Motion Artifacts Dete ction from Computed Tomography Images." Advanced Data Mining Applications ADMA. 347–359.
55. ^Fallenberg L, Dimitrijevic L, Diekmann F (2014). "Impact of Magnification Views on the Characterization of Microcalcifications in Digital Mammography." Röfo.

Supplementary data: available at https://doi.org/10.32388/X7CKJS.3

Declarations

Funding: The authors gratefully acknowledge the partial financial support from the Ministry of Industry and Technology B.14.2.KSG.4.07.00.00-150-1392 and the Akdeniz University Rectorate Scientific Research Center (AU-BAP-FYL1787).

Potential competing interests: No potential competing interests to declare.